Published in final edited form as:
NMR Biomed. 2014 September ; 27(9): 1094–1102. doi:10.1002/nbm.3162.

4D MRI of renal function in the developing mouse

Luke Xie[1,2], **Ergys Subashi**[1,3], **Yi Qi**[1], **Mark A. Knepper**[4], and **G. Allan Johnson**[1,2]

[1]Center for In Vivo Microscopy, Department of Radiology, Duke University Medical Center, Durham, North Carolina 27710

[2]Department of Biomedical Engineering, Duke University, Durham, North Carolina, 27708

[3]Medical Physics Graduate Program, Duke University Medical Center, Durham, North Carolina, 27710

[4]Epithelial Systems Biology Laboratory, National Heart, Lung, and Blood Institute, National Institutes of Health, Bethesda, Maryland, 20892-1603

Abstract

The major roles of filtration, metabolism, and high blood flow make the kidney highly vulnerable to drug-induced toxicity and other renal injuries. A method to follow kidney function is essential for early screening of toxicity and malformations. In this study, we acquired high spatiotemporal resolution (4D) datasets of normal mice to follow changes in kidney structure and function during development. The data were acquired with dynamic contrast-enhanced MRI (via keyhole imaging) and a cryogenic surface coil, allowing us to obtain a full 3D image (125-micron isotropic resolution) every 7.7 seconds over a 50-minute scan. This time course permitted demonstration of both contrast enhancement and clearance. Functional changes were measured over a 17-week course (at 3, 5, 7, 9, 13, and 17 weeks). The time dimension of the MRI dataset was processed to produce unique image contrasts for segmenting the 4 regions of the kidney: cortex (CO), outer stripe (OS) of the outer medulla (OM), inner stripe (IS) of the OM, and inner medulla (IM). Local volumes, time-to-peak (TTP) values, and decay constants (DC) were measured in each renal region. These metrics increased significantly with age, with the exception of DC values in the IS and OS. These data will serve as a foundation for studies of normal renal physiology and future studies of renal diseases that require early detection and intervention.

Keywords

Small animal preclinical imaging; magnetic resonance imaging; magnetic resonance microscopy; mouse kidney development; 3D dynamic contrast enhancement; radial keyhole imaging; cryogenic surface coil

---

Correspondence G. Allan Johnson, Ph.D., Center for In Vivo Microscopy, Department of Radiology, Duke University Medical Center, Box 3302, Durham, NC 27710, Phone: 919 684-7754, Fax: 919 684-7158, gjohnson@duke.edu.

Introduction

The kidney's major role in filtration depends on its high blood flow, concentrating and transport systems, and biochemical activation. These essential features make the kidney highly vulnerable to drug-induced nephrotoxicity and other renal injuries (1-3). A method to follow the dynamic changes in kidney structure and function would be a major advance for noninvasive screening of toxicity and malformations. The normal developmental stages (juvenile to mature adult) provide an important baseline for calibrating functional changes necessary for early detection of renal pathologies (4). However, few tools are available for longitudinal study of kidney structure and function at high resolution.

Diagnostic medical imaging is important for the assessment and management guidance of renal diseases (5-8). Imaging modalities used include ultrasound, x-ray/CT, PET, and MRI, each having its unique attributes and strengths (9,10). Many renal diseases have been studied: polycystic kidney disease by ultrasound (11,12), vascular diseases by CT (13,14), renal cancer by PET (15,16), glomerulosclerosis and age-related nephropathy by MRI (17-20), and inflammation, fibrosis, and toxicity by MRI (21-24). Traditional molecular and urinary biomarkers have been used extensively to assess renal pathophysiology (25-27). Unfortunately, these global metrics are not sensitive and often detect injury too late, when diseases have progressed far beyond intervention (3,6,28,29). Imaging, on the other hand, can monitor and quantitatively assess the onset and progression of renal diseases (6). However, imaging studies have seldom focused on the crucial stage of kidney development when drug-induced toxicity can have the greatest effects. Of the imaging tools that are available, few have been able to study in detail both the structure and function of the entire kidney.

We propose that MRI, with sufficient coverage, contrast, and temporal resolution, can be particularly sensitive in assessing diseases or toxic processes. To calibrate the sensitivity of the method, we acquired high spatiotemporal resolution datasets of the mouse kidney during crucial stages of development. The data were acquired with a cryogenic surface coil and a dynamic contrast-enhanced (DCE) MRI sequence, providing full 3D coverage at microscopic resolution (125^3 μm^3) every 7.7 seconds over a 50-minute scan. This time course allowed demonstration of both inflow and removal of the contrast agent. Structural and functional changes were measured in the kidney over a 17-week course (at 3, 5, 7, 9, 13, and 17 weeks). Specific measurements included local volumes, time-to-peak (TTP) values, and decay constants (DC) in each renal region: cortex (CO), outer stripe (OS) of the outer medulla (OM), inner stripe (IS) of the OM, and inner medulla (IM). To the best of our knowledge, this work demonstrates the first study of the normal development of the mouse kidney using high-resolution MRI.

Methods

Biological support

All animal studies were performed at the Duke Center for In Vivo Microscopy and were approved by the Duke Institutional Animal Use and Care Committee. The protocols adhered to the NIH Guide for the Care and Use of Laboratory Animals.

C57BL/6 mice (n=5, Charles River Laboratories, Wilmington, MA) were imaged longitudinally over a 17-week course (3, 5, 7, 9, 13, 17 weeks). Animals were provided with free access to water before imaging studies. While imaging, the animals were anesthetized under isoflurane and were breathing freely. Three-dimensional printing (Stratasys Dimension, Eden Prairie, MN) was used to make custom parts for the nose cone and for proper positioning of the animal inside the cryogenic surface coil, which was designed for brain imaging.

Gadolinium-based contrast agent (gadofosveset trisodium, Lantheus Medical Imaging, Billerica, MA) was injected as a bolus via tail vein catheter with a dose of 0.03 mmol/kg (similar to clinical dose) and at a rate of approximately 0.35mL/min. Contrast was injected using an automatic syringe pump (KD Scientific, Holliston, MA).

Magnetic resonance imaging (MRI)

MR imaging was performed on a 7 T, 20-cm bore magnet (Bruker BioSpec 70/20 USR, Billerica, MA) interfaced to an Avance III system. The scanner has actively shielded gradients (440 mT/m amplitude) with integrated shims up to 2nd order. A high-sensitivity cryogenic RF coil was used for transmission and reception (Bruker CryoProbe). Due to the small size of the cryoprobe, only one kidney (left kidney, n=5) was imaged and analyzed for all animals.

A custom interleaved radial sequence (center out 3D ultrashort echo time [UTE]) was implemented on Bruker ParaVision 5.1 to allow for keyhole imaging. Thirteen uniform-interleaved subvolumes of Fourier space were sampled (total views=40222, polar undersampling=2, TR=2.5 ms, TE=20 μs, FA=10°, BW=100kHz). Images were reconstructed by sharing the projections from the unique subvolumes via a sliding window approach, a technique known as radial keyhole imaging (30). This yielded a 3D image (160^3 voxels, 125 μm resolution, i.e., voxels of 1.95 nL) every 7.7 sec over a 50-min time course (390 time points) 10th f contrast enhancement and clearance. Contrast agent was injected on the 10th 3D image (77 sec). This point is considered time 0 for subsequent calculations.

This study yielded 160×160×160×390 pixels per scan (6.4 GB) for 5 mice over 17 weeks of development (192 GB). A pre-contrast and a post-contrast image were acquired (160×160×160×104, 1.7 GB each), which were averaged in the time dimension to create enhanced anatomical images. Altogether, a 294 GB dataset was acquired.

Image processing

A bias field correction was applied to reduce inhomogeneities of the B_1 field from the cryogenic surface coil. This bias field was calculated from the additional post-contrast 3D image. The nonparametric non-uniform intensity normalization algorithm (N4ITK, (31)) was used for the correction. The convergence threshold was set at 0.00004 for both the 1st-level (original resolution, up to 500 iterations) and 2nd-level (half the resolution, up to 500 iterations). The entire 4D dataset is corrected by dividing the image at each time point by the bias field (a scalar 3D image).

The 4D datasets were also registered to reduce motion artifacts. This was implemented by registering each 3D image to a common reference image, which was the additional post-contrast 3D image. Images were registered using FSL (FMRIB Software Library, http://www.fmrib.ox.ac.uk/fsl) using correlation ratio, affine transform, hanning sinc interpolation, and a search range of −60 to 60 in all three axes. Typical changes due to registration were: 0.2° for rotation, 150 μm (≈1 pixel) for translation, 0.3% for scale, and 0.3% for skew.

Analysis

Functional maps were determined from the time intensity curves of the DCE datasets. The functional images include a time-to-peak (TTP) map and a decay constant (DC) map. The workflow from an example DCE dataset is shown in Fig. 1. For each pixel in the DCE dataset, the time intensity curve is separated into two parts: 1) the wash-in (transient) phase up to the peak intensity, and 2) the wash-out (tissue) phase after the peak intensity. The transient phase is used to calculate the TTP, or time of injection to peak enhancement. The tissue phase (from time of peak intensity to last time point) is first smoothed using Savitzky-Golay filter (32) with a span of about 7% or 25 time points (calculated in MATLAB, MathWorks, Natick, MA). The filtered data (black lines in intensity curve of Fig. 1) is then used to calculate the DC by fitting a single-term exponential function (Eq. 1). The pixel-wise analysis yielded a 3D TTP and a 3D DC map.

$$y=A \cdot e^{-t/c} \quad (1)$$

where y is the signal intensity, A is the amplitude, t is the time, and c is the decay constant. A small decrease in signal from the tissue phase curve was found in certain areas of the inner medulla (time intensity curve in Fig. 1). This effect was small and occurred in a short period during the time series.

The 4D dataset was also used to produce 3 image contrasts including a temporal sum intensity projection (tSIP), a temporal variance intensity projection (tVIP), and a temporal maximum intensity projection (tMIP). The tSIP, tVIP, and tMIP were determined by computing the sum, variance, and maximum, respectively, at every voxel along the tiem dimension. The tMIP was used to segment the kidney from the background tissue and other organs (via thresholding at 14%). Manual segmentation was used to segment the kidney when thresholding did not work. The inner medulla (IM) was segmented from the tSIP image using seeded region growing inside the IM. Region growing has been demonstrated to segment structures in the kidney (19,24). Lastly, the inner stripe (IS) of the outer medulla (OM) and outer stripe (OS) of the OM were manually segmented from the tVIP image. The cortex (CO) was determined by subtracting the IM, IS, and OS from the kidney region. These image contrasts demonstrated high contrast of the respective renal regions for segmentation. Manual segmentation and volume rendering were implemented in Avizo (Visualization Sciences Group, Burlington, MA).

The segmented regions were then used to determine region volumes and regionspecific functional metrics. ROI measurements (~100 pixels) were taken in order to avoid areas of artifacts in the functional maps. Artifact areas in DC maps may have been due to signal decreases in the tissue phase curve. The measurements determined in this study included: 1) volumes of the IM, IS, OS, CO, and kidney; 2) TTP in the IM, IS, OS, and CO; 3) DC in the IM, IS, OS, and CO; and 4) animal body weights all throughout development at 3, 5, 7, 9, 13, and 17 weeks. Structural changes (region volume and body weight) were fitted to a polynomial function of 2nd order (33). Functional changes (TTP and DC) were fitted to a linear function (1st order polynomial). Error estimates (standard deviation of the error) of the functions were determined at the 95% confidence interval for predicting a future observation. The goodness of fit of the functions was evaluated using an adjusted R^2:

$$R^2_{adjusted}=1-(SS_{resid}/SS_{total})\times((n-1)/(n-d-1)) \quad (2)$$

where SS is the sum of squares, n is the number of observations, and d is the degree of the polynomial (d=1 or d=2 in this study). The f-statistic was determined for each fitted function. One-way ANOVA (analysis of variance) was performed to determine whether the structural and functional measurements changed with age. A significance level of 0.05 or lower (p-value) was used to reject the null hypothesis that the samples from the measurements are drawn from populations with the same mean.

Lastly, the arterial input function was measured in the aorta to determine any significant changes with age. The relative signal change (34,35) was used to measure the arterial input function (Eq. 3).

$$\Delta S(t)=(S(t)-S(0))/S(0) \quad (3)$$

where ΔS is the relative change in signal intensity as a function of time t, S is the signal intensity through the DCE scan, and $S(0)$ is the signal intensity determined from the additional pre-contrast anatomical image.

Histology

Regions identified in MRI were validated with conventional histology of representative kidneys from 17-week old mice (study termination age). Kidneys were sliced in the coronal plane, stored in 10% formalin, embedded in paraffin, and sectioned at 5-μm thickness. Sections were stained with Hematoxylin and Eosin (H&E). Slides were digitally scanned using brightfield contrast on an Axioskop 2 FS microscope (Carl Zeiss Microscopy, Thornwood, NY). Images were acquired at 1.02 μm using a 10× objective and tiling was required to cover the entire kidney section. Correction was applied to remove the shading effects and non-uniformities in the tiled images. MR images were manually registered (translation, rotation, and scaling) to histology images to enable comparison and confirmation of region segmentation. The identified regions in MRI and histology were confirmed by a renal physiologist (M.A.K.) and a board-certified veterinary pathologist (B.R.B.).

Results

The overview of the datasets for this study is shown in Fig. 2. The first row shows the developmental progression of the kidney (3 to 17 weeks). The second row shows the time series in the DCE dataset (7.7 sec to 50 min). The third row shows the volume image acquired at each time point. Representative slices are shown from the 3D image (160×160×160 voxels).

Image contrasts

Three image contrasts were determined from the time dimension of the DCE dataset (Fig. 3). The tSIP showed the best delineation between the IM and the remaining kidney tissue (Fig. 3A). The tVIP displayed excellent contrast between the OM (IS and OS) and the remaining kidney regions (Fig. 3B). The boundary between the IS and OS is also visible in the tVIP image. An additional layer (bright band) in the most lateral part of the IM can also be seen in the tVIP image (Fig. 3B). This additional layer is not visible in the tSIP image or tMIP image. The tMIP showed the best delineation between the entire kidney and the background tissue (Fig. 3C). The renal regions (CO, OS, IS, IM) were confirmed with histology (Fig. 3D and 3E). The tVIP image is used as the example MRI in Fig. 3D. The identified regions correspond with that of the tSIP and tMIP images.

Structure and function

The structure and function of the kidney are determined from the segmented regions and the functional maps (Fig. 4). The renal regions (CO, OS, IS, IM) were segmented from the respective image contrasts (tSIP, tVIP, and tMIP). The kidney layers are overlaid on a tVIP image (Fig. 4A) and shown as volume renderings (Fig. 4B). The TTP map is shown in Fig. 4C. The DC map is shown in Fig. 4D. The TTP values (in seconds) increased sequentially from the CO to OS to IS to IM. The DC values (in minutes) were not sequential compared to TTP values. The shortest DC values (fastest decay) are found in the IS and OS regions. The longest DC values (slowest decay) are found in the IM. Intermediate DC values can be seen in the CO.

Kidney development

The structural and functional changes of the kidney with age (3, 5, 7, 9, 13, and 17 weeks) are shown in log plots in Fig. 5. Region volumes of the kidney, CO, OS, IS, and IM are shown in Fig. 5A and 5B. The animal body weight was measured (Fig. 5C). The TTP values of the CO, OS, IS, and IM are shown in Fig. 5D. The DC values are shown in Fig. 5E. All measurements increased with age. The volume of the regions increased from the IM to IS to OS to CO. The total volume of the kidney is the summation of all 4 regions. The TTP values also increased sequentially from the IM to IS to OS to CO. However, the DC values were not sequential. The lowest DC values (fastest decay) were found in the IS or OS depending on the age, followed by the CO and then the IM (slowest decay).

The developmental structural changes were modeled by a 2nd-order polynomial function. The developmental functional changes were modeled with a linear function. The bands surrounding the fitted functions show the 95% confidence intervals (Fig. 5). The fitted functions, adjusted residuals, and *f*-statistics are included in tables: region volumes (Table 1), TTP (Table 2), and DC (Table 3). The polynomial function determined for the animal body weight was: $y=-7.17x^2+223x+416$ ($y=10^{-2}$ g, x=age in weeks, $R^2_{\text{adjusted}}=0.964$, *f*-statistic= 67.0). The lowest residual values were found in the DC fitted functions of the IS ($R^2_{\text{adjusted}}=0.741$) and OS ($R^2_{\text{adjusted}}=0.815$). In general, the f-statistics were largest when a linear function was used to fit functional measurements (TTP and DC) and the f-statistics were largest when a polynomial function was used to fit structural measurements (region volume and body weight).

ANOVA tests were performed to determine whether measurements changed significantly with age. All region volumes (IM, IS, OS, CO, kidney) changed significantly with age (p values << 0.01). Animal body weight changed significantly with age (p<<0.01). All region TTP values changed significantly with age (p<0.01). DC values of the IM and CO changed significantly with age (p<0.01). However, DC values of the IS (p=0.11) and the OS (p=0.39) did not change significantly with age. ANOVA tables and boxplots of an example renal region are included in Supplemental Tables and Figures (see Supporting Information).

Since the dynamics of enhancement and clearance depend on the arterial input function, we measured the relative signal intensity change in the aorta of all mice across the 17 weeks of development. We did not find an appreciable difference in the arterial input function as a function of age.

Discussion

In this study, we were able to assess the kidney during the early stages of development (17-week course). We evaluated the structure of the kidney at high resolution (125-μm isotropic) and determined the kidney's function with high temporal resolution (7.7 sec). The unique contrast mechanisms of MRI and image processing in the time dimension (tSIP, tVIP, and tMIP) allowed us to segment four layers of the kidney in 3D (CO, OS, IS, and IM). Measurements were determined throughout development and demonstrated that this crucial stage was indeed a very sensitive age span for large changes in structure and function. This was determined by ANOVA tests where kidney measurements changed significantly from week 3 to week 17, with the exception of DC values in the IS and OS.

One particular image contrast, the tVIP, created an additional layer in the IM that was not visible in the histology image. This layer had the brightest intensity because it had the highest variance along the time dimension. The high variance suggests a unique functionality of this kidney area that is quite different from the structure identified in histology. The finding was consistent in tVIP images across animals and across age. One possible explanation is the smaller interstitial space compared to the rest of the IM and the smaller amount of hyaluronan in this area compared to the papilla, i.e., the deepest part of IM (36). This allows the contrast agent to move quickly in and out of the region and thus have a large signal intensity variation with time.

Structural and functional changes with age

Renal region volumes increased monotonically with age, following a 2^{nd}-order polynomial function. TTP and DC values increased monotonically with age, following a linear function. The biggest region was the CO, followed by the OS, IS, and IM. The rate of growth was fastest in the CO but slowest in the IS, which was the second smallest region throughout development. The rate of growth was similar in the IM, IS, and OS compared to the CO. The growth rate of the kidney (summation of all regions) was similar to the growth rate of the animal body, considering the volume ratio of the kidney to the body. The peak enhancement was fastest (smallest TTP) in the CO, followed by the OS, IS, and IM (biggest TTP) at all ages. This is expected considering the sequential function of the kidney starting with filtration in the CO and eventual excretion in the IM and renal papilla. The TTP values increased with age in all kidney regions, demonstrating a slower regional enhancement with age. The clearance of contrast agent was fastest (smallest DC) in the IS and OS with significant overlap throughout development. The intermediate DC values were measured in the CO and the slowest clearance (biggest DC) was found in the IM. The slowest clearance in the IM can be expected, since the IM is the last to enhance and the last to clear the entire contrast agent passing through the kidney. All clearance rates (DC values) in renal regions increased with age, which demonstrate a slower removal of contrast agent. The increase of TTP and DC with age suggest longer enhancement times, longer clearance times, and potentially declining renal function. The decrease of renal function can be related to general renal aging pattern, a decrease in glomerular filtration rate, a decrease in tubular function, and a loss of urine-concentrating ability (37,38).

DC values in the IS and OS did not change significantly with age. These same regions (IS and OS) were the slowest in volumetric growth rate with age (based on the polynomial function). The IS and OS also have the 2nd and 3rd fastest increase of TTP values with age. The IS and OS have the fastest clearance rates based on DC values. The DC value did not increase or decrease sequentially from the CO to OS to IS to IM, which was distinctly different from the sequential pattern in region volumes or TTP values. The IS and OS were the most distinct layers for both structure and function.

There are several reasons that can explain the fast clearance rates (small DC values) in the IS and OS. One must first consider the time scales. During the wash-in phase, TTP values were less than 2 min in all renal regions. During this time span, the fast dynamics can be related to simple filtration and secretion (39). During the wash-out phase, DC values ranged from 40 to 180 min. These dynamics are much slower and are related to many more processes. The second consideration is the size of the contrast agent. The contrast agent (Gadofosveset trisodium) has a small size of 957 Da or < 1 nm (40,41) and can go through filtration, secretion, and extravasation. Filtration occurs via glomeruli in the cortex, secretion occurs via proximal tubules, and extravasation occurs via vasa recta in the medulla. The ascending vasa recta are highly fenestrated (42) allowing the contrast agent to escape the vascular lumen and enter the medullary interstitium. Unlike the OM (IS and OS) interstitium, the IM interstitium is filled with glycosaminoglycan, hyaluronan, and other polymers (43). The contrast agent can interact or be hindered by these molecules in the IM and be cleared the slowest compared to the IS and OS. The IM interstitial space is also much greater volumetrically than the OM (36). This results in a greater residence time, which would further slow down the removal of the contrast agent in the IM (bigger DC value). The absence of interacting molecules and the smaller interstitial space in the OM (IS and OS) allowed for fast clearance rates in this region.

Study comparison

Kidney function has been measured with DCE-MRI previously. Baumann et al. (44) demonstrated similar sequential TTP increasing from the CO to OM to IM in a rat kidney. DCE-MR images were acquired at a resolution of 400×400×1200 μm^3 (192 nL) every 6 sec. A wide variety of contrast agents have been used to study renal function with MRI, e.g., Gd-DOTA, Gadofosveset trisodium, and Gd-dendrimers (45). Gadofosveset trisodium has one of the highest relaxivities (46) and has been used to study renal function with DCE-MRI in pigs (47) and rats (48). In the later study, the time intensity curves (wash-out phase) were fitted with an exponential function to compare DC values for a normal kidney and a disease model. Images were acquired at 313×625×2000 μm^3 (391 nL) every 20 sec. Significant advances have been made for DCE-MRI in imaging of tumor models. the highest isotropic resolution DCE-MRI was achieved at 156×156×156 μm^3 One of (3.81 nL) every 9.9 sec (30). One of the fastest DCE-MRI, while maintaining good spatial resolution, was achieved at 391×391×2000 μm^3 (305 nL) every 1.5 sec (49). To the best of our knowledge, few studies, if any, have been able to distinguish the IS and OS volumetrically, assess renal function in all four regions, and achieve isotropic resolution of 125 μm (1.95 nL) every 7.7 sec.

Kidney function has been assessed with traditional biomarkers. One such biomarker is glomerular filtration rate (GFR) using EDTA, serum creatinine, or inulin (50,51). GFR has been used to follow functional changes with age. Hackbarth et al. (38) showed a decline in renal function (decreasing GFR) with age in C57BL/6 mice. Here, the measured GFR was 1.61, 1.39, 1.12, and 0.94 mL/min/180g body weight at 9.6, 29, 66, and 101 weeks, albeit at a period later than the present study. Very few, if any, studies have assessed the kidney during early development (3 to 17 weeks). GFR, however, is not a perfect metric and can be inaccurate for chronic and acute renal diseases (6,28). MRI, on the other hand, can determine renal function in local areas, evaluate renal structure, and measure MR-based GFR with the right tools and techniques (52).

Technical considerations

One of the limitations of the present study arises from the use of the cryogenic surface coil. The non-uniform excitation (B_1) makes it difficult to calibrate T_1 changes required to map gadolinium concentrations. Accurate concentrations are necessary for kinetic modeling, rate constants, and MR-based GFR. The major benefit of the cryoprobe is a much higher SNR allowing us to obtain very high spatiotemporal resolutions. We exploited the high spatiotemporal resolution to determine regional TTP and DC values, which do not require measurements of concentration. Even with a 7.7-sec sampling time, the temporal resolution is marginal, especially during wash-in (transient) phase of contrast enhancement in the CO. TTP values, which were determined from the transient phase, increased from 13.5 sec (week 3) to 21.7 sec (week 17) in the CO during development. These values are very close to multiples of our 7.7-sec sampling period and the limited sampling during this rapidly changing inflow limits the precision of these measurements. Spatial resolution is equally important in determining local TTP values; temporal resolution is only in part related to the accuracy of DCE-MRI quantification (53). Every experiment involves a trade off between time (temporal resolution or acquisition time), spatial resolution, coverage, and SNR. The multidimensional nature of this study forces a number of tradeoffs. The shortest TTP encountered in this study is ~14 sec in the CO at 3 weeks. The longest TTP (~110 sec) is seen in the IM at 17 weeks. And the decay constant in the IM at 17 weeks is nearly 11000 sec (180 min). So while there is limited sampling for the most rapidly changing physiology, the protocol spans an enormous range of temporal change.

Lastly, additional work is needed to understand the effects of undersampling and keyhole reconstruction of DCE-MRI for the kidney. Namely, is it valid to share views of k-space with 13 keys while maintaining the image fidelity of kidney structure and function, or can more keys be shared? For instance, increasing the number of keys can increase the temporal resolution; however, more k-space periphery is shared from other views. Keyhole imaging can be implemented with a variation of k-space cutoff frequencies via filtering strategies (54). Together, the number of keys and filtering strategies can affect temporal resolution, spatial resolution, and sampling artifacts (30).

Conclusion

The data acquired here provides a comprehensive assessment of the normal development in the mouse kidney at 6 age points, 390 dynamic time points, and 160×160×160 spatial points. The high spatiotemporal resolution 4D images will be especially important for comparing nephrotoxicity models and disease models with heterogeneous abnormalities, such as chronic kidney disease and polycystic kidney disease. These diseases require early detection and intervention before the kidney becomes fully developed and damages become irreversible. The structural and functional measurements can also be used for studies of normal renal physiology.

Representative 3D datasets and Supporting Information are available via CIVMSpace, our method for sharing information with the scientific community (http://www.civm.duhs.duke.edu/lx201403).

Acknowledgments

The authors wish to thank the following individuals at Duke University: Patrick McGuire and Nikhil Bumb for 3D printing assistance at the Mechanical Engineering and Materials Science department; Dr. Laurence W. Hedlund for assistance with animal use protocols; Dr. John C. Nouls for assistance for MRI; Dr. Zackary I. Cleveland for scientific discussions; and Sally Zimney for editorial assistance. The authors also thank Brian R. Berridge (GlaxoSmithKline) for histological insight.

Sponsors

This work was supported by the NIH/NIBIB national Biomedical Technology Resource Center (P41 EB015897 to G.A.J.).

List of abbreviations

ANOVA	Analysis of variance
CO	Cortex
DC	Decay contrast

DCE	Dynamic contrast enhancement
GFR	Glomerular filtration rate
IM	Inner medulla
IS	Inner stripe
OM	Outer medulla
OS	Outer stripe
tMIP	Temporal maximum intensity projection
tSIP	Temporal sum intensity projection
TTP	Time-to-peak
tVIP	Temporal variance intensity projection
UTE	Ultrashort echo time

References

1. Samiy AH. Renal disease in the elderly. The Medical clinics of North America. 1983; 67(2):463–480. [PubMed: 6338324]
2. Thadhani R, Pascual M, Bonventre JV. Acute renal failure. The New England journal of medicine. 1996; 334(22):1448–1460. [PubMed: 8618585]
3. Trof RJ, Di Maggio F, Leemreis J, Groeneveld AB. Biomarkers of acute renal injury and renal failure. Shock. 2006; 26(3):245–253. [PubMed: 16912649]
4. Meneton P, Ichikawa I, Inagami T, Schnermann J. Renal physiology of the mouse. American journal of physiology Renal physiology. 2000; 278(3):F339–351. [PubMed: 10710537]
5. Rahbari-Oskoui F, Mittal A, Mittal P, Chapman A. Renal relevant radiology: radiologic imaging in autosomal dominant polycystic kidney disease. Clinical journal of the American Society of Nephrology: CJASN. 2014; 9(2):406–415. [PubMed: 24370765]
6. Bae KT, Grantham JJ. Imaging for the prognosis of autosomal dominant polycystic kidney disease. Nature reviews Nephrology. 2010; 6(2):96–106.
7. George SM, Kalantarinia K. The role of imaging in the management of cardiorenal syndrome. International journal of nephrology. 2011:245241. 2011. [PubMed: 21318046]
8. Zagoria RJ. Imaging of small renal masses: a medical success story. AJR American journal of roentgenology. 2000; 175(4):945–955. [PubMed: 11000140]
9. Ettlin RA. Toxicologic pathology in the 21st century. Toxicologic pathology. 2013; 41(5):689–708. [PubMed: 23143188]
10. Ying X, Monticello TM. Modern imaging technologies in toxicologic pathology: An overview. Toxicologic pathology. 2006; 34(7):815–826. [PubMed: 17178685]
11. Gabow PA. Autosomal dominant polycystic kidney disease. The New England journal of medicine. 1993; 329(5):332–342. [PubMed: 8321262]
12. Parfrey PS, Bear JC, Morgan J, Cramer BC, McManamon PJ, Gault MH, Churchill DN, Singh M, Hewitt R, Somlo S, Reeders ST. The diagnosis and prognosis of autosomal dominant polycystic kidney disease. The New England journal of medicine. 1990; 323(16):1085–1090. [PubMed: 2215575]
13. Nordsletten DA, Blackett S, Bentley MD, Ritman EL, Smith NP. Structural morphology of renal vasculature. American journal of physiology Heart and circulatory physiology. 2006; 291(1):H296–309. [PubMed: 16399870]

14. Bentley MD, Ortiz MC, Ritman EL, Romero JC. The use of microcomputed tomography to study microvasculature in small rodents. American journal of physiology Regulatory, integrative and comparative physiology. 2002; 282(5):R1267–1279.
15. Hoh CK, Seltzer MA, Franklin J, deKernion JB, Phelps ME, Belldegrun A. Positron emission tomography in urological oncology. The Journal of urology. 1998; 159(2):347–356. [PubMed: 9649238]
16. Schoder H, Larson SM. Positron emission tomography for prostate, bladder, and renal cancer. Seminars in nuclear medicine. 2004; 34(4):274–292. [PubMed: 15493005]
17. Bennett KM, Zhou H, Sumner JP, Dodd SJ, Bouraoud N, Doi K, Star RA, Koretsky AP. MRI of the basement membrane using charged nanoparticles as contrast agents. Magnetic resonance in medicine: official journal of the Society of Magnetic Resonance in Medicine/Society of Magnetic Resonance in Medicine. 2008; 60(3):564–574.
18. Chevalier RL. Chronic partial ureteral obstruction and the developing kidney. Pediatr Radiol. 2008; 38(Suppl 1):S35–40. [PubMed: 18071697]
19. Xie L, Cianciolo RE, Hulette B, Lee HW, Qi Y, Cofer G, Johnson GA. Magnetic resonance histology of age-related nephropathy in the Sprague Dawley rat. Toxicologic pathology. 2012; 40(5):764–778. [PubMed: 22504322]
20. Egger C, Cannet C, Gerard C, Debon C, Stohler N, Dunbar A, Tigani B, Li J, Beckmann N. Adriamycin-induced nephropathy in rats: Functional and cellular effects characterized by MRI. Journal of magnetic resonance imaging: JMRI. 2014
21. Farmer TH, Johnson GA, Cofer GP, Maronpot RR, Dixon D, Hedlund LW. Implanted coil MR microscopy of renal pathology. Magnetic resonance in medicine: official journal of the Society of Magnetic Resonance in Medicine/Society of Magnetic Resonance in Medicine. 1989; 10(3):310–323.
22. Hedlund LW, Maronpot RR, Johnson GA, Cofer GP, Mills GI, Wheeler CT. Magnetic resonance microscopy of toxic renal injury induced by bromoethylamine in rats. Fundam Appl Toxicol. 1991; 16(4):787–797. [PubMed: 1884916]
23. Williams JB, Ye Q, Hitchens TK, Kaufman CL, Ho C. MRI detection of macrophages labeled using micrometer-sized iron oxide particles. Journal of magnetic resonance imaging: JMRI. 2007; 25(6):1210–1218. [PubMed: 17520727]
24. Xie L, Sparks MA, Li W, Qi Y, Liu C, Coffman TM, Johnson GA. Quantitative susceptibility mapping of kidney inflammation and fibrosis in type 1 angiotensin receptor-deficient mice. NMR in biomedicine. 2013; 26(12):1853–1863. [PubMed: 24154952]
25. Esson ML, Schrier RW. Diagnosis and treatment of acute tubular necrosis. Annals of internal medicine. 2002; 137(9):744–752. [PubMed: 12416948]
26. Bellomo R, Ronco C, Kellum JA, Mehta RL, Palevsky P. Acute Dialysis Quality Initiative w. Acute renal failure - definition, outcome measures, animal models, fluid therapy and information technology needs: the Second International Consensus Conference of the Acute Dialysis Quality Initiative (ADQI) Group. Critical care. 2004; 8(4):R204–212. [PubMed: 15312219]
27. Tonelli M, Sacks F, Pfeffer M, Jhangri GS, Curhan G. Cholesterol, Recurrent Events Trial I. Biomarkers of inflammation and progression of chronic kidney disease. Kidney international. 2005; 68(1):237–245. [PubMed: 15954913]
28. Ferguson MA, Vaidya VS, Bonventre JV. Biomarkers of nephrotoxic acute kidney injury. Toxicology. 2008; 245(3):182–193. [PubMed: 18294749]
29. Grantham, JJ.; Welling, LW.; Edwards, RM. Comprehensive Physiology. John Wiley & Sons, Inc.; 2010. Evaluation of Function in Single Segments of Isolated Renal Blood Vessels, Nephrons, and Collecting Ducts.
30. Subashi E, Moding EJ, Cofer GP, MacFall JR, Kirsch DG, Qi Y, Johnson GA. A comparison of radial keyhole strategies for high spatial and temporal resolution 4D contrast-enhanced MRI in small animal tumor models. Med Phys. 2013; 40(2):022304. [PubMed: 23387766]
31. Tustison NJ, Avants BB, Cook PA, Zheng Y, Egan A, Yushkevich PA, Gee JC. N4ITK: improved N3 bias correction. IEEE Trans Med Imaging. 2010; 29(6):1310–1320. [PubMed: 20378467]
32. Orfanidis, SJ. Introduction to signal processing. Prentice Hall; Englewood Cliffs, N.J.: 1996. p. xvip. 798

33. Michielsen K, Meersschaert J, De Keyzer F, Cannie M, Deprest J, Claus F. MR volumetry of the normal fetal kidney: reference values. Prenatal diagnosis. 2010; 30(11):1044–1048. [PubMed: 20734348]
34. Jones RA, Easley K, Little SB, Scherz H, Kirsch AJ, Grattan-Smith JD. Dynamic contrast-enhanced MR urography in the evaluation of pediatric hydronephrosis: Part 1, functional assessment. AJR American journal of roentgenology. 2005; 185(6):1598–1607. [PubMed: 16304021]
35. Bokacheva L, Rusinek H, Chen Q, Oesingmann N, Prince C, Kaur M, Kramer E, Lee VS. Quantitative determination of Gd-DTPA concentration in T1-weighted MR renography studies. Magnetic resonance in medicine: official journal of the Society of Magnetic Resonance in Medicine/Society of Magnetic Resonance in Medicine. 2007; 57(6):1012–1018.
36. Knepper MA, Danielson RA, Saidel GM, Post RS. Quantitative analysis of renal medullary anatomy in rats and rabbits. Kidney international. 1977; 12(5):313–323. [PubMed: 604620]
37. Burich RL. Effects of age on renal function and enzyme activity in male C57BL/6 mice. Journal of gerontology. 1975; 30(5):539–545. [PubMed: 127007]
38. Hackbarth H, Harrison DE. Changes with age in renal function and morphology in C57BL/6, CBA/HT6, and B6CBAF1 mice. Journal of gerontology. 1982; 37(5):540–547. [PubMed: 7096924]
39. Steinhausen M. [A method for the differentiation of proximal and distal tubuli in the renal cortes in vivo and its use in determining tubular flow rates]. Pflugers Archiv fur die gesamte Physiologie des Menschen und der Tiere. 1963; 277:22–35.
40. Caravan P, Cloutier NJ, Greenfield MT, McDermid SA, Dunham SU, Bulte JW, Amedio JC Jr. Looby RJ, Supkowski RM, Horrocks WD Jr. McMurry TJ, Lauffer RB. The interaction of MS-325 with human serum albumin and its effect on proton relaxation rates. Journal of the American Chemical Society. 2002; 124(12):3152–3162. [PubMed: 11902904]
41. Eldredge HB, Spiller M, Chasse JM, Greenwood MT, Caravan P. Species dependence on plasma protein binding and relaxivity of the gadolinium-based MRI contrast agent MS-325. Investigative radiology. 2006; 41(3):229–243. [PubMed: 16481905]
42. Schwartz MM, Karnovsky MJ, Vehkatachalam MA. Ultrastructural differences between rat inner medullary descending and ascending vasa recta. Laboratory investigation; a journal of technical methods and pathology. 1976; 35(2):161–170.
43. Knepper MA, Saidel GM, Hascall VC, Dwyer T. Concentration of solutes in the renal inner medulla: interstitial hyaluronan as a mechano-osmotic transducer. American journal of physiology Renal physiology. 2003; 284(3):F433–446. [PubMed: 12556362]
44. Baumann D, Rudin M. Quantitative assessment of rat kidney function by measuring the clearance of the contrast agent Gd(DOTA) using dynamic MRI. Magnetic resonance imaging. 2000; 18(5): 587–595. [PubMed: 10913720]
45. Grenier N, Pedersen M, Hauger O. Contrast agents for functional and cellular MRI of the kidney. European journal of radiology. 2006; 60(3):341–352. [PubMed: 16973326]
46. Rohrer M, Bauer H, Mintorovitch J, Requardt M, Weinmann HJ. Comparison of magnetic properties of MRI contrast media solutions at different magnetic field strengths. Investigative radiology. 2005; 40(11):715–724. [PubMed: 16230904]
47. Ludemann L, Nafz B, Elsner F, Grosse-Siestrup C, Meissler M, Kaufels N, Rehbein H, Persson PB, Michaely HJ, Lengsfeld P, Voth M, Gutberlet M. Absolute quantification of regional renal blood flow in swine by dynamic contrast-enhanced magnetic resonance imaging using a blood pool contrast agent. Investigative radiology. 2009; 44(3):125–134. [PubMed: 19151609]
48. Zhang Y, Choyke PL, Lu H, Takahashi H, Mannon RB, Zhang X, Marcos H, Li KC, Kopp JB. Detection and localization of proteinuria by dynamic contrast-enhanced magnetic resonance imaging using MS325. Journal of the American Society of Nephrology: JASN. 2005; 16(6):1752–1757. [PubMed: 15872075]
49. Loveless ME, Halliday J, Liess C, Xu L, Dortch RD, Whisenant J, Waterton JC, Gore JC, Yankeelov TE. A quantitative comparison of the influence of individual versus population-derived vascular input functions on dynamic contrast enhanced-MRI in small animals. Magnetic resonance

in medicine: official journal of the Society of Magnetic Resonance in Medicine/Society of Magnetic Resonance in Medicine. 2012; 67(1):226–236.

50. Levey AS, Bosch JP, Lewis JB, Greene T, Rogers N, Roth D. A more accurate method to estimate glomerular filtration rate from serum creatinine: a new prediction equation. Modification of Diet in Renal Disease Study Group. Annals of internal medicine. 1999; 130(6):461–470. [PubMed: 10075613]
51. Mogensen CE. Glomerular filtration rate and renal plasma flow in short-term and long-term juvenile diabetes mellitus. Scandinavian journal of clinical and laboratory investigation. 1971; 28(1):91–100. [PubMed: 5093523]
52. Jones RA, Votaw JR, Salman K, Sharma P, Lurie C, Kalb B, Martin DR. Magnetic resonance imaging evaluation of renal structure and function related to disease: technical review of image acquisition, postprocessing, and mathematical modeling steps. Journal of magnetic resonance imaging: JMRI. 2011; 33(6):1270–1283. [PubMed: 21590995]
53. Rosen MA, Schnall MD. Dynamic contrast-enhanced magnetic resonance imaging for assessing tumor vascularity and vascular effects of targeted therapies in renal cell carcinoma. Clinical cancer research: an official journal of the American Association for Cancer Research. 2007; 13(2 Pt 2): 770s–776s. [PubMed: 17255308]
54. Song HK, Dougherty L. Dynamic MRI With Projection Reconstruction and KWIC Processing for Simultaneous High Spatial and Temporal Resolution. Magnetic Resonance in Medicine. 2004; 52:815–824. [PubMed: 15389936]

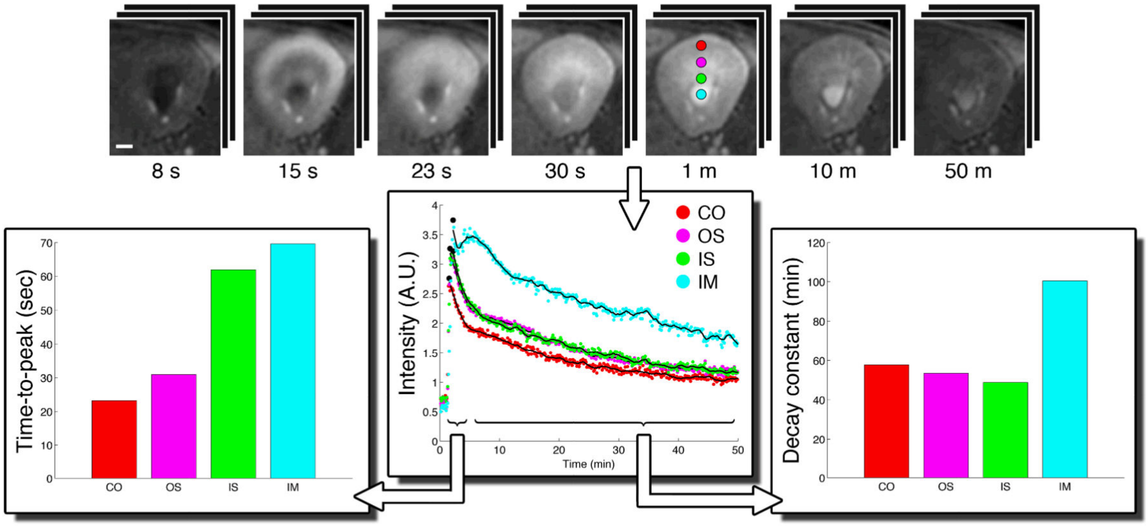

Figure 1.

Example DCE dataset shown at a 7 time points (out of 390) in an axial view. Time intensity curves shown for 4 renal regions: cortex (CO), outer stripe (OS), inner stripe (IS), and inner medulla (IM). Filtered intensity curves (black line) are shown for the wash-out (tissue) phase. The time-to-peak is determined from the wash-in (transient) phase and the decay constant is determined from the wash-out (tissue) phase. Scale bar = 1 mm.

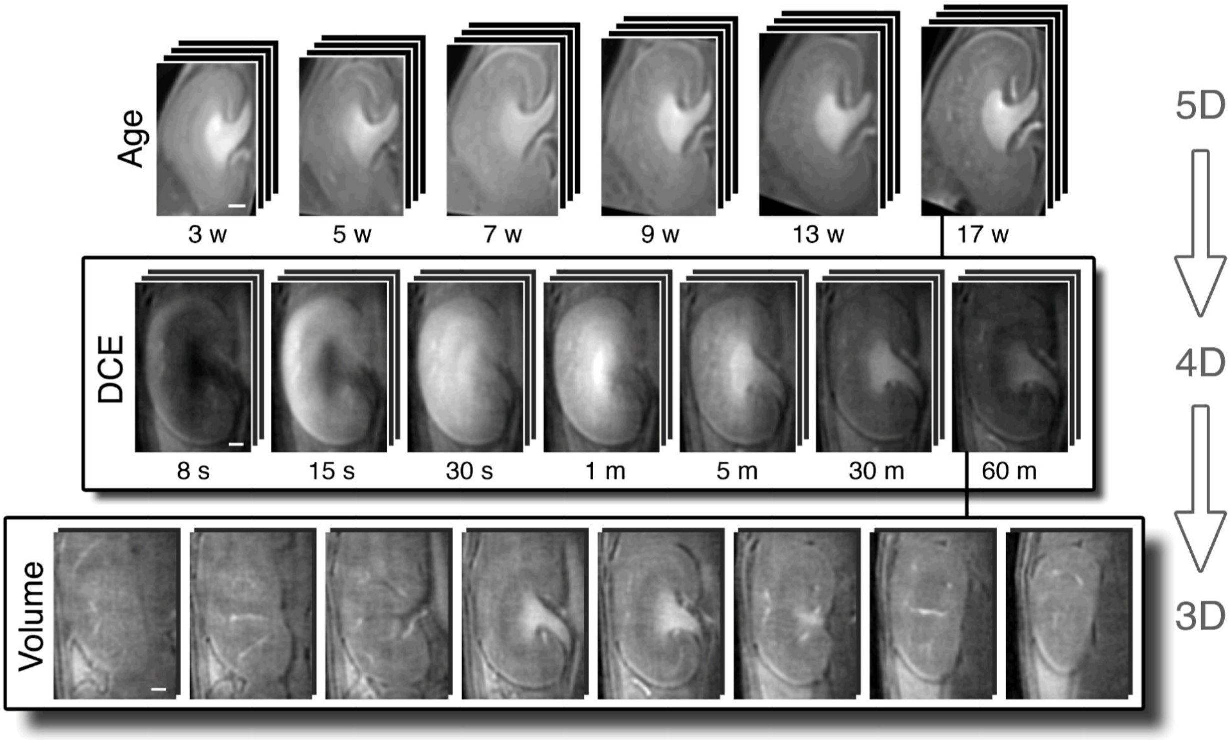

Figure 2.

Overview of the data. First row: Animals (n=5) were imaged over 17 weeks of development (at 3, 5, 7, 9, 13, and 17 weeks). Second row: Representative time points from the DCE dataset (390 time points) at one age. Third row: Representative slices from the DCE dataset at one time point. Scale bars = 1 mm. The mouse head is towards the top of the image.

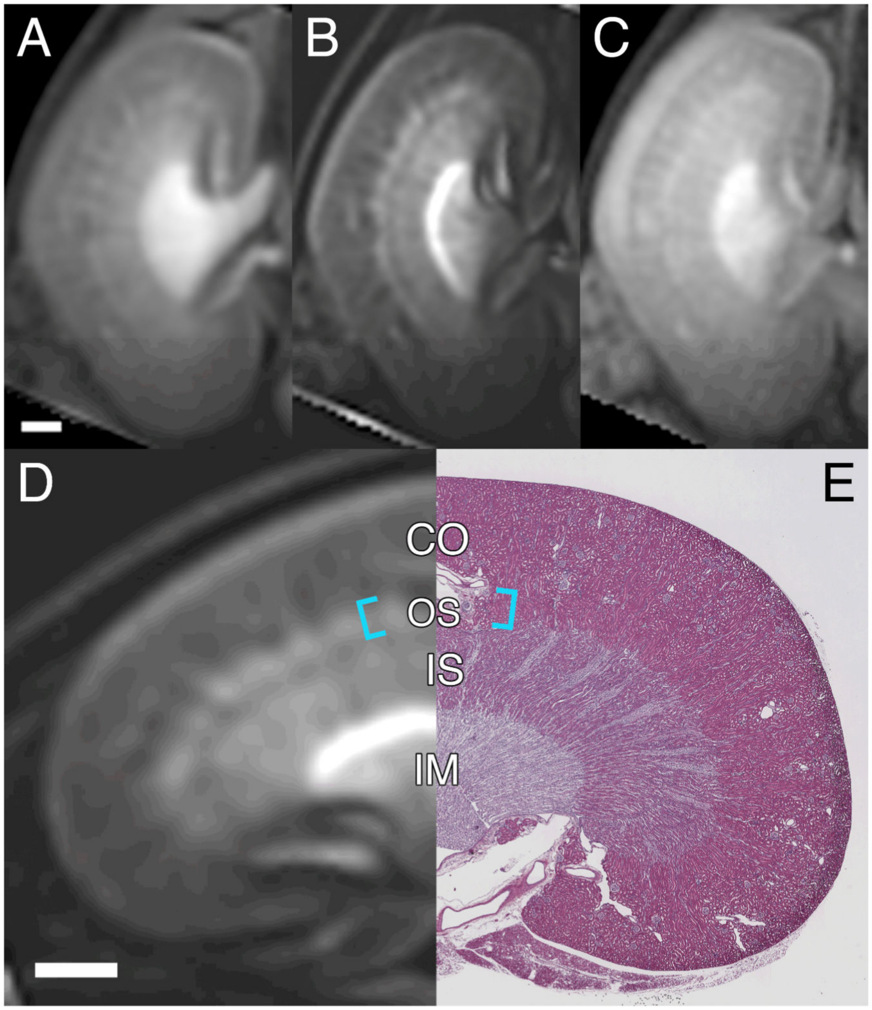

Figure 3.

Three image contrasts produced from the DCE dataset. A: Temporal sum intensity projection (tSIP). B: Temporal variance intensity projection (tVIP). C: Temporal maximum intensity projection (tMIP). Aligned tVIP image (D) with H&E histology image (E). Labeled regions include cortex (CO), outer stripe (OS) of the outer medulla (OM), inner stripe (IS) of the outer medulla (OM), and inner medulla (IM). Cyan brackets indicate the OS. Scale bars = 1 mm.

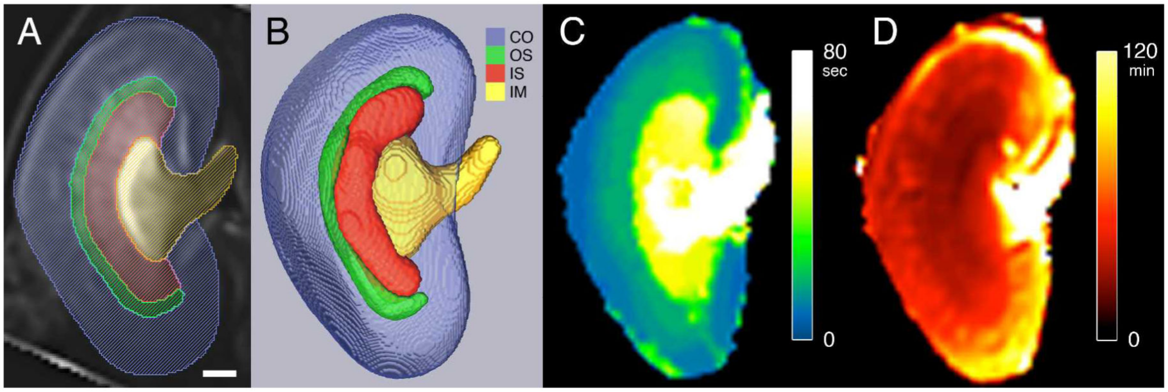

Figure 4.

Segmented renal structures and functional maps. Segmented regions overlaid on a tVIP MRI (A) and volume rendering of regions (B). Regions shown in A and B: cortex (CO, blue), outer stripe (OS, green), inner stripe (IS, red), and inner medulla (IM, yellow). C: Time-to-peak (TTP) map. D: Decay constant (DC) map. Scale bar = 1 mm.

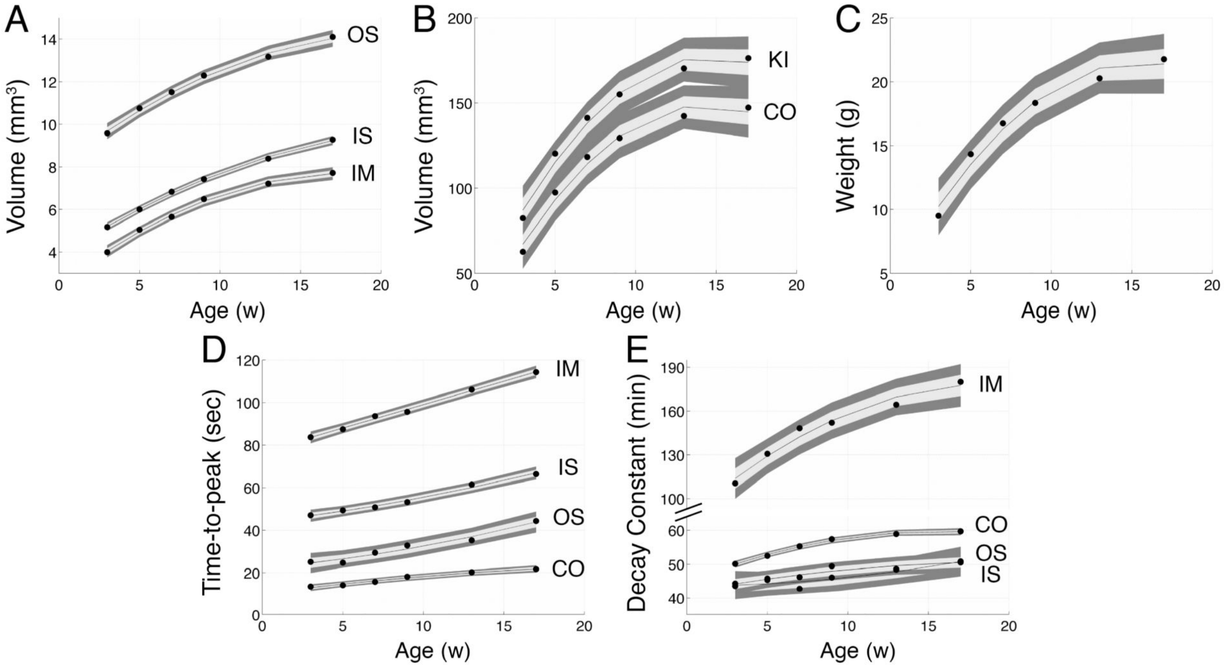

Figure 5.

Plots showing kidney development with age. Measured regions: kidney (KI), cortex (CO), outer stripe (OS), inner stripe (IS), and inner medulla (IM). A-B: Region volumes. C: Animal body weight. D: Time-to-peak values. E: Decay constants. measurements (region volume and body weight) are fitted with a 2nd-order polynomial function (black line in A-C). Functional measurements (TTP and DC) are fitted to a linear function (black line in D-E). The gray band shows the 95% confidence interval.

Table 1

Polynomial fit of 2nd order of age (weeks) to region volume (mm^3).

	Polynomial function (mm^3, 10^{-2})	**Adjusted residuals**	***f*-statistic**
Inner medulla	$-1.63x^2 + 58.7x + 243$	0.994	402
Inner stripe	$-0.99x^2 + 48.7x + 383$	0.997	960
Outer stripe	$-1.42x^2 + 59.4^{x} + 803$	0.992	327
Cortex	$-62.6x^2 + 1810x + 1850$	0.971	83.7
Kidney	$-65.9x^2 + 1940x + 3480$	0.976	103

Table 2

Linear fit of age (weeks) to region time-to-peaks (sec).

	Linear function (sec, 10^{-2})	**Adjusted residuals**	***f*-statistic**
Inner medulla	$220x + 7700$	0.994	775
Inner stripe	$144x + 4180$	0.976	205
Outer stripe	$138x + 1960$	0.942	82.9
Cortex	$63.0x + 1160$	0.961	126

Table 3

Linear fit of age (weeks) to region decay constant (min).

	Linear function (min, 10^{-2})	**Adjusted residuals**	***f*-statistic**
Inner medulla	$452x + 10700$	0.904	48.1
Inner stripe	$49.8x + 4170$	0.741	15.3
Outer stripe	$44.8x + 4350$	0.815	23.1
Cortex	$67.5x + 4960$	0.849	29.2